Supporting Information

Understanding the Effects of Binder Dissolution Dynamics on the Chemistry and Performance of Lithium-Sulfur Batteries

Saheed A. Lateef[1], John Chmiola[2], Fabio Albano[2], William E. Mustain[1], and Golareh Jalilvand[1]*

[1]*Department of Chemical Engineering, University of South Carolina, Columbia, SC 29208, USA*

[2]*NantG Power LLC, El Segundo, CA 90245, USA*

*Corresponding Author: jalilvand@sc.edu

Authors Information

Corresponding Author

Golareh Jalilvand – Department of Chemical Engineering, University of South Carolina, Columbia, SC 29208, USA
Phone: +1-803-576-8359
Email: jalilvand@sc.edu

Authors

Saheed A. Lateef – Department of Chemical Engineering, University of South Carolina, Columbia, SC 29208, USA
Email: slateef@email.sc.edu

John Chmiola – NantG Power LLC, El Segundo, CA 90245, USA
Email: john.chmiola@nantgpower.com

Fabio Albano – NantG Power LLC, El Segundo, CA 90245, USA
Email: Fabio.albano@nantgpower.com

William E. Mustain – Department of Chemical Engineering, University of South Carolina, Columbia, SC 29208, USA
Email: mustainw@mailbox.sc.edu

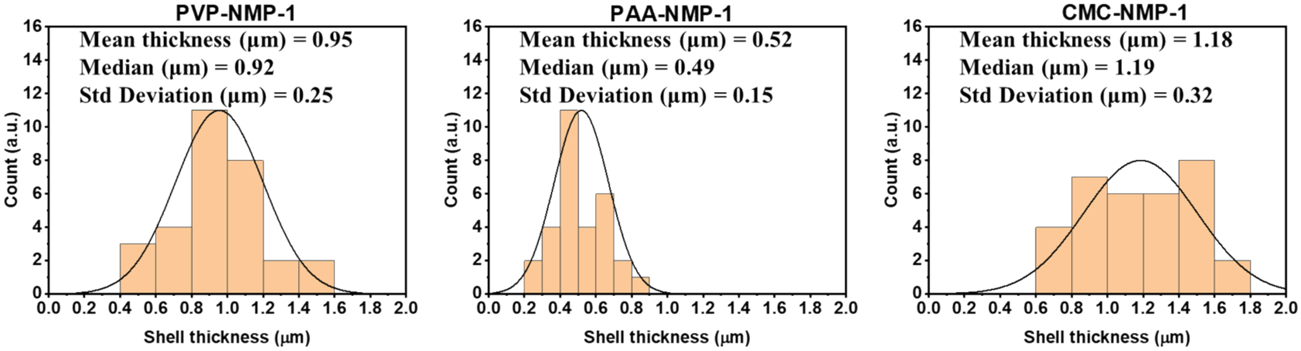

Figure S1: Distribution of shell thickness surrounding sulfur particles in group 1 electrodes.

Measurements were taken for approximately 30 particles per sample. The mean shell thicknesses were found to be 0.95 μm for PVP, 0.52 μm for PAA, and 1.18 μm for CMC. These results reinforce the proposed mechanism linking binder–solvent interaction strength to shell morphology. Specifically, the thinner and less stable shells observed with PAA are attributed to its strong hydrogen bonding with NMP, which promotes rapid dissolution and poor adsorption onto the particle surface. In contrast, PVP and CMC form thicker shells due to more moderate or limited solvation, enabling greater retention on the particle surface. The slightly thicker shells in CMC are attributed to the strong intra-chain hydrogen bonding and a more compact, rigid conformation of CMC chains, which delays the dissolution of the binder, as shown and discussed with FTIR results.

Table S1: The value of the overpotential (ΔV) obtained for cells in groups 1 and 3 obtained from subtraction of discharge peak potential from that of the charge potential peak from the dQ/dV vs V plots.

Cells	1^{st} cycle (mV)	20^{th} cycle (mV)	50^{th} cycle (mV)
PVP-NMP-1	314	314	314
PAA-NMP-1	428	427	427
CMC-NMP-1	254	253	253
PVP-NMP-3	312	311	311
PAA-NMP-3	426	427	427
CMC-NMP-3	179	179	178

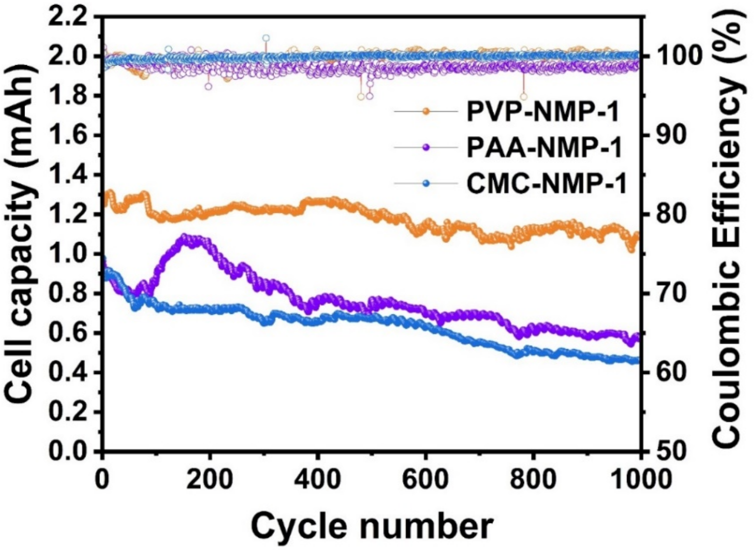

Figure S2: Long cycle life performance of Group 1 cells.

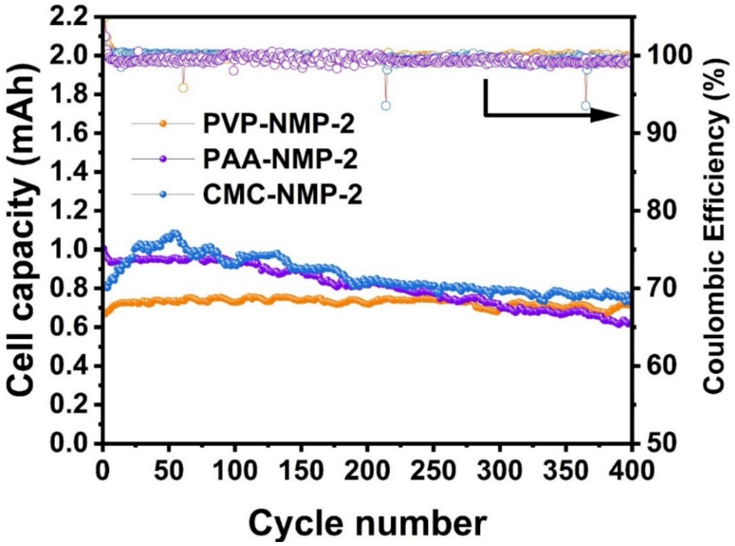

Figure S3: The capacity retention of the Group 2 cells.

The shell-free PAA-NMP-2 electrode showed the highest initial capacity compared to PVP-NMP-2 and CMC-NMP-2, indicating that the shells might momentarily impede the proper access of electrolyte to the sulfur active material to some extent (either electrically or ionically). However, the difference of the initial capacities of the electrodes with different binders was not significant. The PVP-NMP-2 maintained a stable capacity at 0.83 mAh for 400 cycles, despite its inhomogeneous shell structure (Figure 1d). This is while PAA with similar inhomogeneity (Figure 1e) in its shell structure did not perform efficiently, indicating that the efficiency of the shells depends on both their morphology, and the intrinsic properties of its binder.

The discharge capacity of CMC-NMP-2 was fairly stable, despite some initial instability up to the first 50th cycle. Yet, it showed a slightly higher capacity loss (from 1.07 mAh at the 50th cycle to 0.72 mAh at the 400th cycle) compared to PVP-NMP-2, which is in confirmation with the results in Group 1. On the other hand, the shell-free PAA-NMP-2 experienced the highest decay in the discharge capacity from 1.00 mAh in the 1st cycle to 0.62 mAh at the 400th cycle, which confirmed the impact of binder shells on impeding the loss of polysulfides.

Definition of terms:

Q_H is the capacity contribution of the electrodes from 2.8 V to 2.1 V. Q_L is the capacity obtained by subtracting the Q_H from the total capacity of the electrode at that cycle.

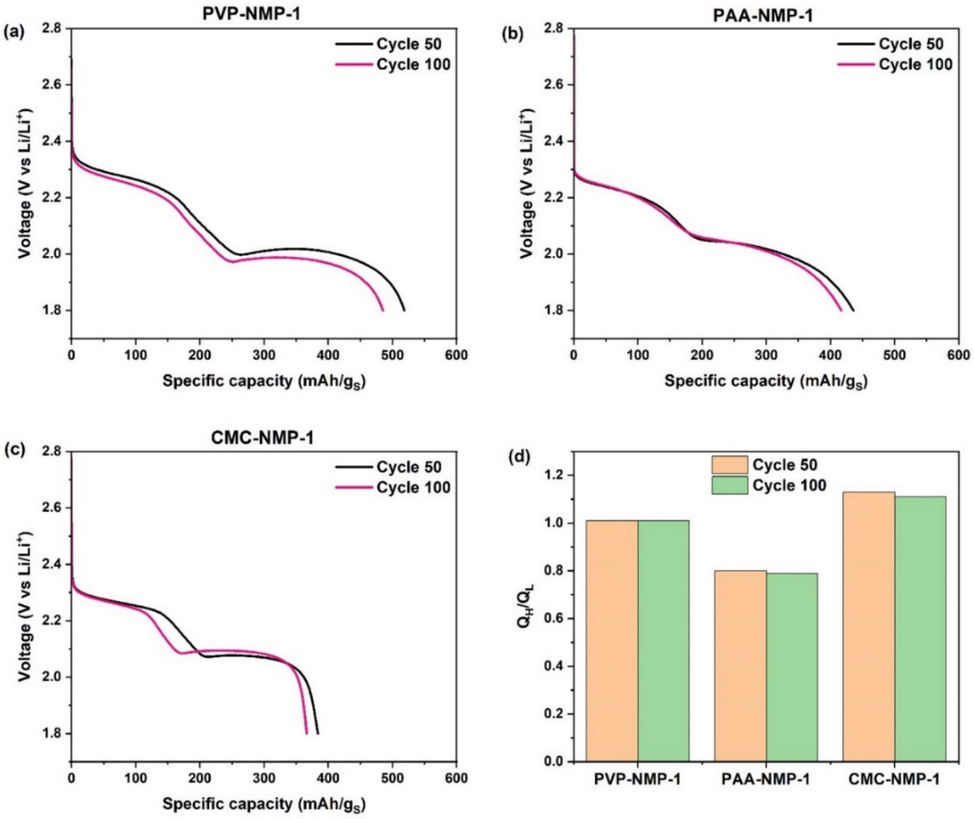

Figure S4: Discharge profiles of the Group 1 electrodes with NMP solvent at cycles 50 and 100, showing the contribution of each of the plateaus to the total discharge capacity. (a) PVP-NMP-1 (b) PAA-NMP-1 and (c) CMC-NMP-1. (d) Q_H/Q_L of (a)-(c) with 50th cycle in orange bars and 100th cycle in green bars.

Two signature discharge plateaus for LSB were observed in all electrodes, yet with different lengths. The quantified Q_H/Q_L values are presented in Table S2, particularly highlighting their change upon cycling. The Q_H/Q_L ratio was fairly constant from the 50th cycle to 100th cycle for the electrodes with uniform shell coverings around the sulfur particles. Specifically, the PVP-NMP-1 cathode (Figure S4a) had a highly stable performance as its Q_H/Q_L remained unchanged at 1.01 from the 50th cycle to the 100th cycle. The Q_H/Q_L of the CMC-NMP-1 cathode (Figure S4c) changed only for 0.01 from 50 to 100 cycles. This is while the PAA-NMP-1 had a Q_H/Q_L change of 0.04 in the same cycling duration, as seen in Figure S4b. Figure S4d compares the values of all Q_H/Q_L at 50th and 100th cycles at a glance.

The stable Q_H/Q_L in the PVP- and CMC-based electrodes with distinct shell coverings around the sulfur particles confirmed the ability of the shells to assist with impeding polysulfides from leaving the cathode. This suggests that the lower overall capacity retention in CMC-NMP-1 electrode is likely due to other characteristics of the CMC binder such as the abundant Na^+ groups in its structure, especially at a high degree of substitution of 0.9, which can provide a better host for the deposition of the negatively charged and insulating solid LiPS products, resulting in gradual insulation of the active surface areas in sulfur cathode, and decay in capacity.

Similarly for the groups 2 cells, the loss of active material through polysulfide dissolution was quantified using the Q_H/Q_L values and presented in Table S2. The Q_H/Q_L from the 50th cycle to 100th cycle in PVP-NMP-2 and CMC-NMP-2 electrodes with shell coverings only changed by 0.04 and 0.08, respectively. The larger drops in the Q_H/Q_L values from Group 1 to Group 2 was in confirmation with partially deteriorating shells in PVP-NMP-2 electrode and notably thinner shells in CMC-NMP-2 electrode. The larger loss of active material in CMC was also in agreement with the Group 1 observations. In the same cycle duration PAA-NMP-2 displayed the highest drop of 0.5 in its Q_H/Q_L value. These results were manifested in the overall capacity retention of the cells as well. After 400 cycles, the PVP-NMP-2 cell resulted in a 90% capacity retention, followed by CMC-NMP-2 cell with 67%, and PAA-based electrode with 55% (Figure S3). PAA-NMP-2 lacked the advantage of shells in trapping polysulfide and capacity retention, showing the highest capacity loss. The above observation on the role of shell covering in impeding polysulfide movement is also confirmed by the results of group 3 cells where a noticeable and relatively comparable reduction in the Q_H/Q_L value from the 50th cycle to 100th cycle showing a 0.4, 0.5 and 0.4 drop in PVP-NMP-3, PAA-NMP-3, and CMC-NMP-3, respectively occurs (Table S2). In summary, the capacity retention of the cells becomes poorer from group 1 to 3 as the shell covering gets degraded.

The nearly constant Q_H/Q_L from the 50^{th} cycle to the 100^{th} cycle in the group 1 cathodes indicates that the soluble polysulfides produced at high potential plateau are preserved for subsequent cycles. This preservation of the polysulfides leads to accessibility at subsequent cycles due to the physical entrapment by the shells. These numbers are not significantly preserved for the groups 2 and 3 cells where the sulfur particle shell covering are gradually decomposing into complete degradation in group 3 cells.

Table S2: The high and low potential plateau capacities in the discharge process at 50th and 100th cycles for the NMP-processed Group 1-3 electrodes.

	50th cycle			100th cycle		
	Q_H	Q_L	Q_H/Q_L	Q_H	Q_L	Q_H/Q_L
PVP-NMP-1	259.92	258.43	1.01	243.72	241.31	1.01
PAA-NMP-1	192.26	242.60	0.79	183.9	242.27	0.75
CMC-NMP-1	203.20	180.52	1.13	187.84	168.43	1.12
PVP-NMP-2	206.11	199.55	1.03	199.44	202.20	0.99
PAA-NMP-2	301.25	130.33	2.31	272.92	153.11	1.78
CMC-NMP-2	240.42	266.18	0.90	225.13	273.35	0.82
PVP-NMP-3	128.26	70.50	1.82	110.25	78.78	1.40
PAA-NMP-3	143.13	86.53	1.65	104.49	88.81	1.18
CMC-NMP-3	263.87	148.86	1.77	214.50	149.72	1.43

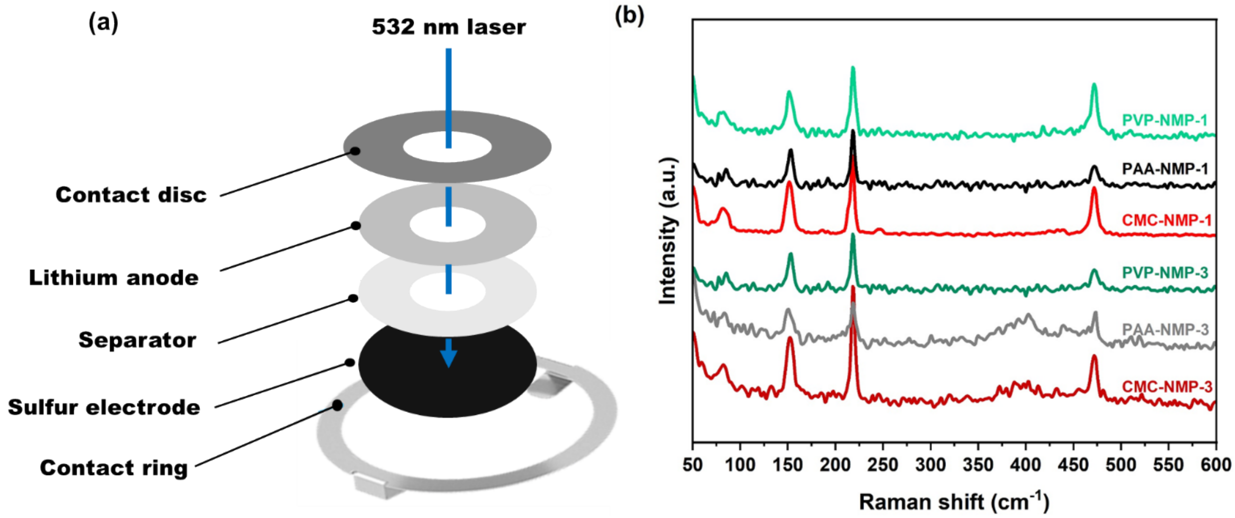

Figure S5: (a) Schematic of the EL-cell assembly for *in-situ* Raman measurement. (b) The Raman spectra of the electrodes before cycling reveal distinct features.

The Raman spectra of the cells before cycling show various peaks at asymmetric sulfur bending moment (152 cm^{-1}, 219 cm^{-1}) and symmetric bending at 473 cm^{-1} indicating the presence of S_8.

Table S3: References used for Raman peak assignment

Species	Measurements (this study)	Literature assignment + refs
S_8^{2-}	154, 222, 474	154, 220, 475[1] 155, 219, 478[2]
S_6^{2-}	401–403	399.5[1]
S_4^{2-}	456–457	455[3]
$S_6^{2-} + S_4^{2-}$	401	400[4], 405[5]

Note: The peak positions are in cm^{-1} unit.

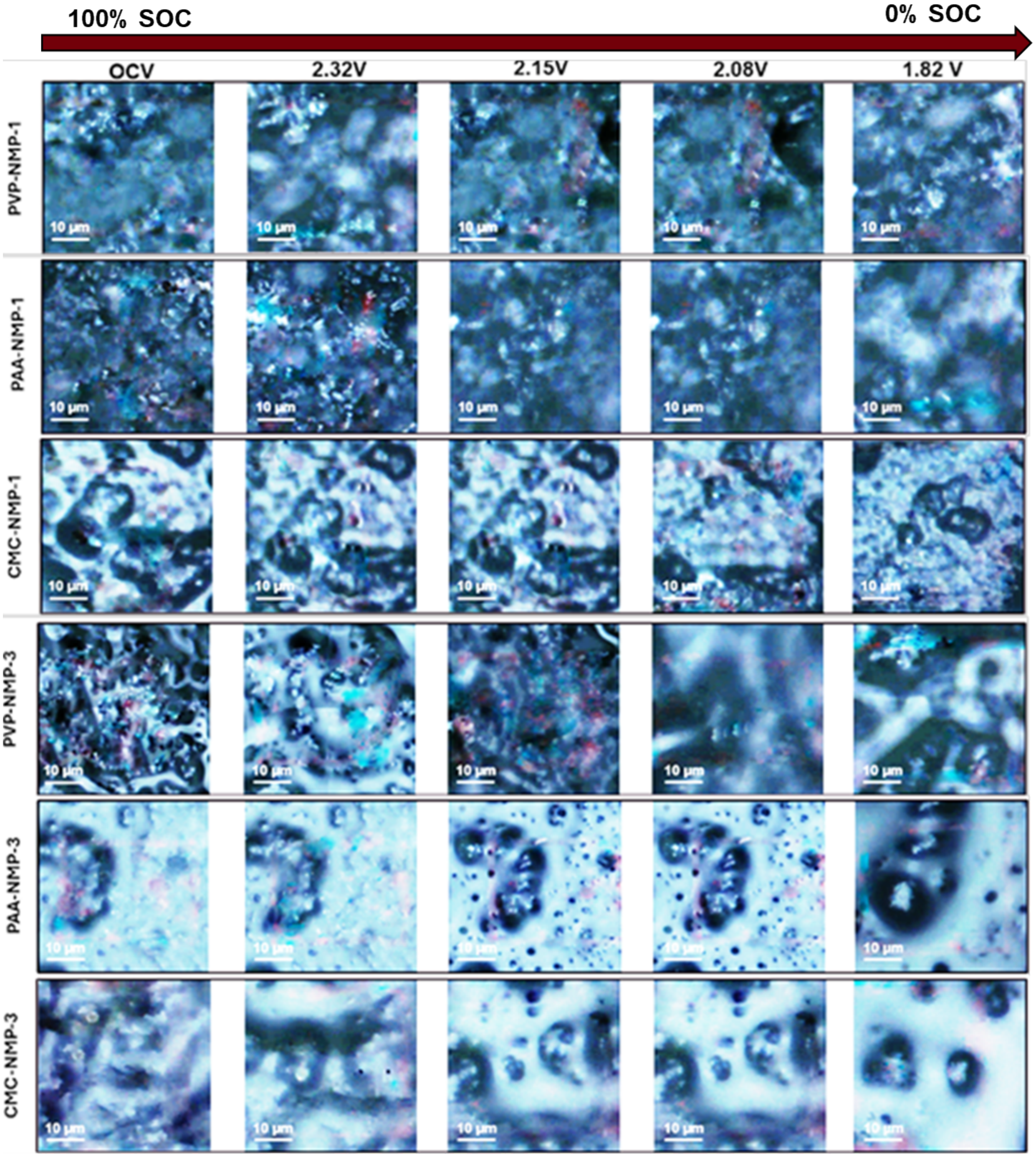

Figure S6: The optical images of the sulfur electrodes taken during operando Raman experiments. The optical images of the electrodes at each potential where Raman spectra were collected are shown in Figure 5 and compared with images before cycling (at OCV).

The surface of the electrodes with unshelled particles (PVP-NMP-3, PAA-NMP-3 and CMC-NMP-3) showed significant evolution upon discharge due to free polysulfide dissolution below 2.15 V. By progressing towards lower SOCs at the end of the discharge process (1.82 V), solid discharge products deposited on the surface. This notable change in the electrodes surface is in agreement with the relatively lower capacity retention of Group 3 electrodes, confirming the uncontrolled dissolution of polysulfides in those cells, thus their notable deposition on the surface of the cathode at the end of discharge. On the other hand, the electrodes with shelled particles showed significantly less changes in their surface upon discharge, compared to Group 3 electrodes. Among shelled electrodes, PVP-NMP-1 electrode showed the least change from 100-0% SOC, which supports its excellent capacity retention. These results combined with the *in-situ* Raman observations validate the effect of binder shell morphology around sulfur particles in constraining the polysulfide within cathode and controlling the shuttling mechanism.

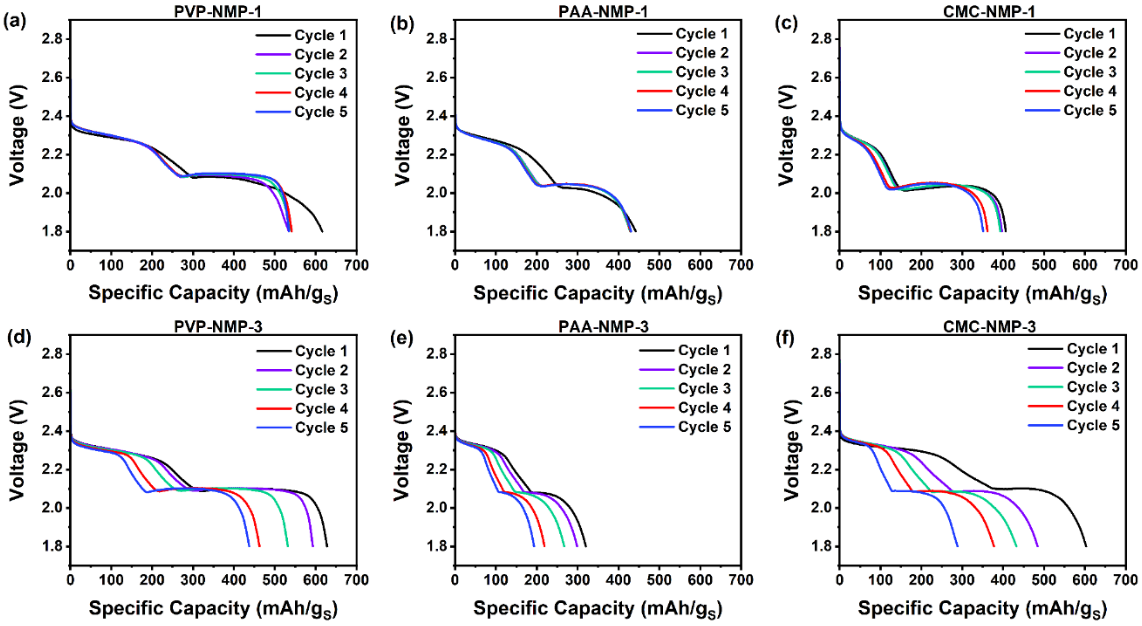

Figure S7: Discharge curves of the sulfur cathodes during a cumulative 4-day resting period for the cells with shelled and un-shelled particles. Cycle 1 indicates the initial discharge capacity from where the initial high potential plateau capacity, C_{Hi}, was extracted. Each of cycles 2-5 were the capacities obtained after resting for 24 h at 100% state of charge and the subsequent C_{Hs} were obtained. This means that Cycle 2 was obtained after the first 24 h of rest after first charge. Similarly, cycles 3-5 are after 2nd-4th 24 h resting period, respectively. The high potential plateaus at each cycle were used to calculate self-discharge constant, k_s according to this equation $C_H = C_{H_i} e^{-(\frac{k_s}{t})}$.

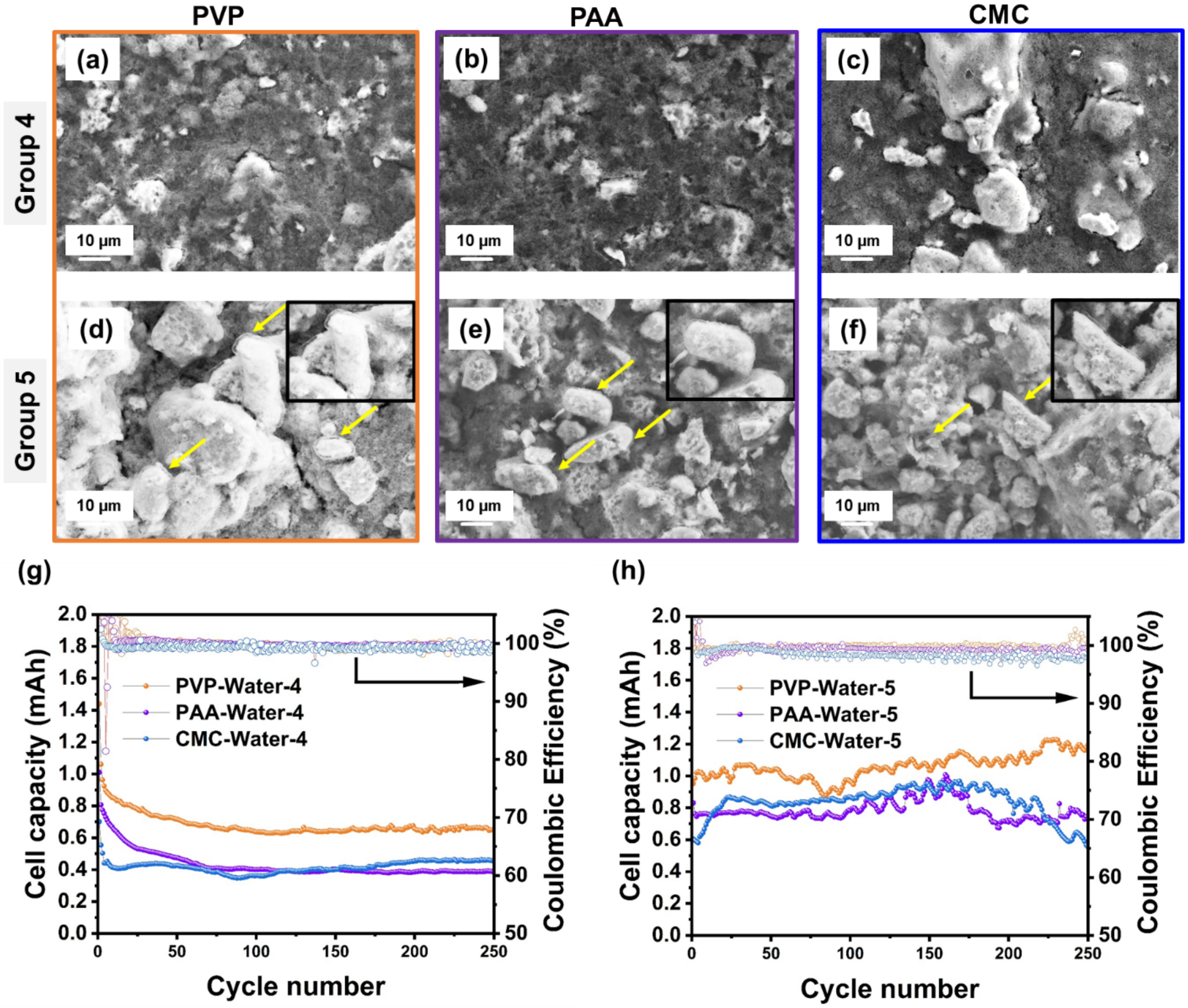

Figure S8: SEM images and capacity retention of Group 4 and 5 electrodes with (a, d) PVP, (b, e) PAA and (c, f) CMC binders, dissolved in water instead of NMP. Group 4 electrodes were prepared similar to Group 1 only by replacing NMP with water. Group 5 had the same recipe as Group 4, only with 1/5 of the tiring time (5 hours). Shells are pointed at by arrows and shown in inset images of the water-based cathodes for Groups 4 and 5 electrodes.

With the increasing demand for green solvent due to toxicity and cost of NMP, development of water-soluble binders is on the increase. It is also important to demonstrate the concept presented in this article on the impact of morphological difference due to controlled binder dissolution, using water as the binder. The dissolution process was approached as shown for group 1 where the contact time between the binder and the solvent was 1 day (Group 4). No shell covering was observed on the particle (Figure S8 a-c) for all the binders. Going by the observations and deductions made so far, decreasing the dissolution time would control the binder solubility which would preserve the formation of the shell. To achieve that, shorter dissolution/stirring time of 5h was used. Shorter times such as 1h and 2 h were too short to achieve any homogeneous slurry due to the hydrophobic nature of carbon. At 5 h stirring time (Group 5), the electrodes had particles covering in shells (Figure S8 d-f), even though the size of the shell and the relative number of particles covered is different than what was observed in Group 1 electrodes. We attribute this variation to the readiness of water to participate in hydrogen bonding which could hasten the binder dissolution and degrade the shell if the stirring time is prolonged.

The morphological differences in Group 4 and Group 5 electrodes also manifest in the capacity retention where the group 4 electrodes (Figure S8g) had much more inferior retention (45% for PVP, 38% for PAA and 64% for CMC) than Group 5 (Figure S8h) with at least 90% capacity retention for the three binders. A decreasing value of the ratio of Q_H/Q_L was also observed going from Group 4 cells (Figure S9) to Group 5 cells (Figure S10). While it does not invalidate the observation on the capacity retention, the unstable capacity in the cells with 5h of stirring could be due to hydrophobic nature of carbon that makes the ink not completely homogeneous.

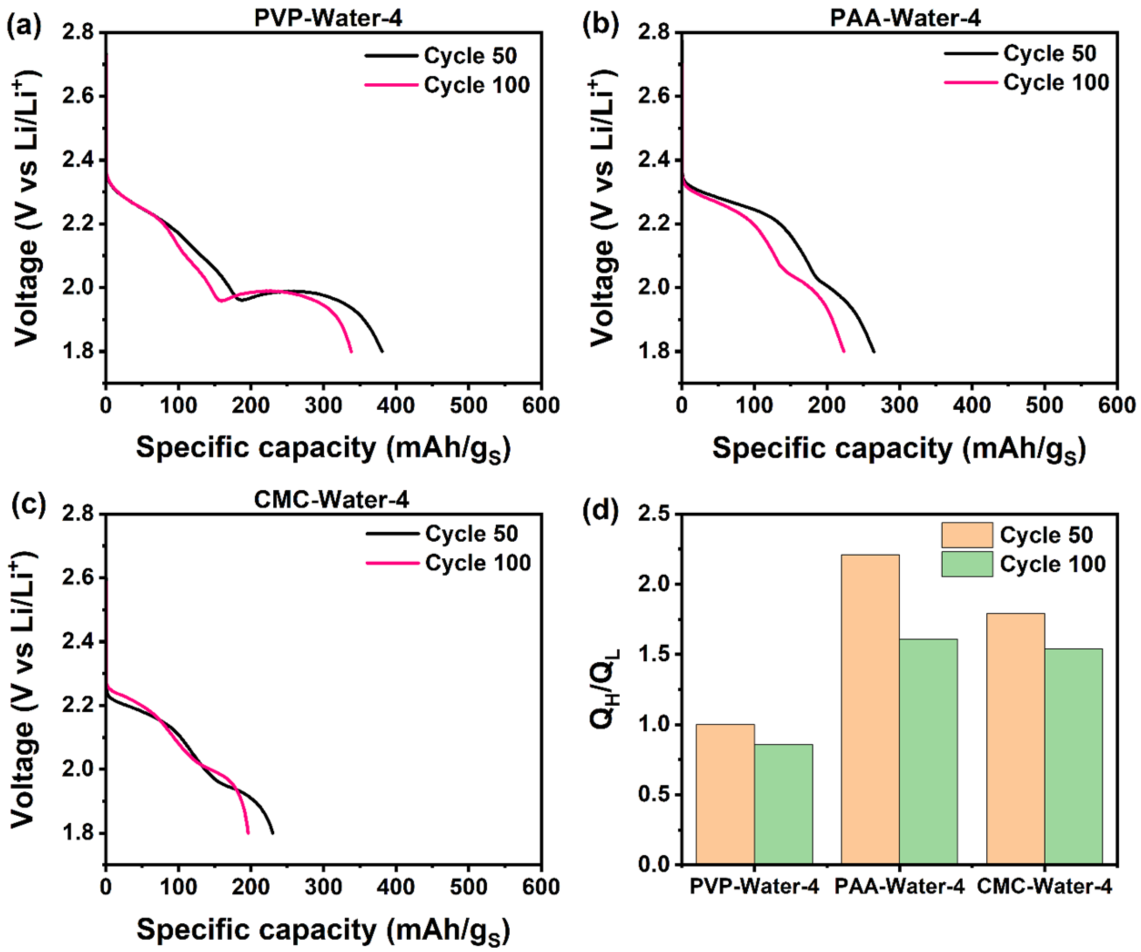

Figure S9: Discharge profiles of the Group 1 electrodes with NMP solvent at cycles 50 and 100, showing the contribution of each of the plateaus to the total discharge capacity. (a) PVP-Water-4 (b) PAA-Water-4 and (c) CMC-Water-4. (d) Q_H/Q_L of (a)-(c) with 50th cycle in orange bars and 100th cycle in green bars

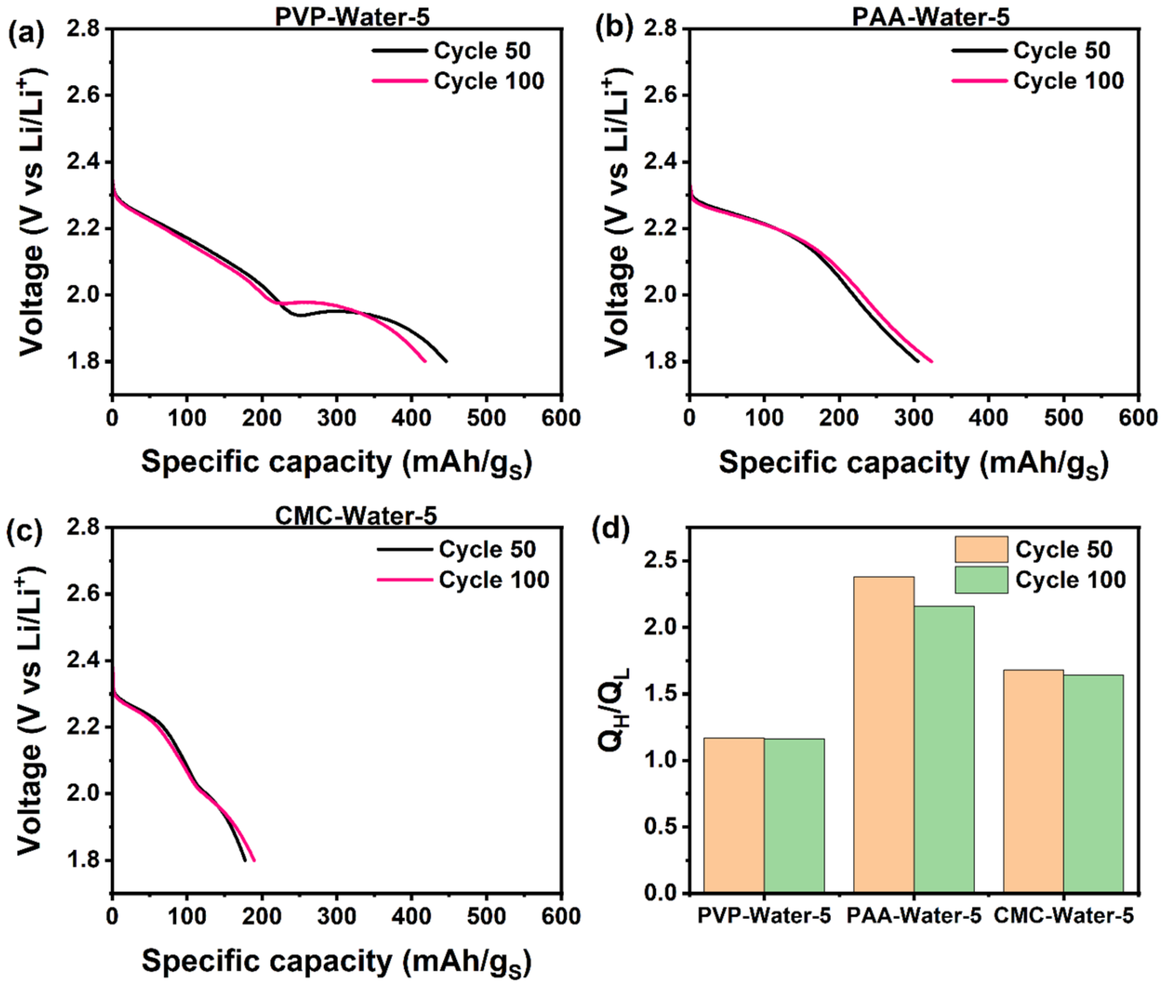

Figure S10: Discharge profiles of the Group 1 electrodes with NMP solvent at cycles 50 and 100, showing the contribution of each of the plateaus to the total discharge capacity. (a) PVP-Water-5 (b) PAA-Water-5 and (c) CMC-Water-5. (d) Q_H/Q_L of (a)-(c) with 50th cycle in orange bars and 100th cycle in green bars

Table S4: Table shows the contribution of the lower potential plateau relative to the high potential plateau to the overall discharge capacity in the discharge process at 50th and 100th cycles for Ketjen-based electrodes at low and high sulfur loadings.

	50^{th} cycle			100^{th} cycle		
	Q_H	Q_L	Q_H/Q_L	Q_H	Q_L	Q_H/Q_L
PVP-KJ-NMP-L	315.12	615.12	0.51	296.24	603.81	0.49
PVP-KJ-NMP-H	238.79	476.25	0.50	248.07	474.92	0.51

Table S5: Comparison of the present work demonstrating the achievement of polysulfide trapping binder shell confinements solely through the optimization of binder dissolution behavior—without any chemical modification—using low-cost, commercially available binders with other common reports focusing on chemical and functional modification of binders.

Binder	**Capacity** (mAh/g)	**Retention** (%)	**Sulfur loading** (mg/cm^2)	**E/S** (µL/mg$_S$)	**# of cycles**	**C-rate**	**Refs**
ZIP	1200	83	–	–	100	0.2	[1]
PPA	900	83	1.2	35	100	0.2	[2]
PVP	601	74	1.1–1.3	60	50	0.1	[6]
PDADMA	875	77	–	–	65	0.2	[7]
PEI	730	82	2.4	–	300	0.5	[8]
PVS	1100	68	5.0	20	100	0.5	[9]
LSBP	996	80	1.6	–	300	0.1	[10]
AHP	920	81	–	–	200	0.5	[11]
GA-CNF	1100	90	1.1	–	250	0.1	[12]
SPI-PAM	1258	71	2.3	–	200	0.5	[13]
PVP	825	90	1.1	10	250	0.1	This work

PDADMA = polydiallyldimethylammonium; PVS = poly(vinyl sulfate) potassium salt ; ZIP = Zwitterionic Polymer; LSBP = lithiophilic and sulfiphilic bifunctional polymer; AHP = novel copolymer whose name was not revealed; PPA = hyperbranched polymer obtained from polymerization reaction of poly(ethylene glycol) diglycidyl ether with polyethylenimine; GA-CNF = Gum Arabic deposited onto carbon nanofiber interlayer; SPI-PAM = binder obtained from double cross linked soy protein isolate (SPI)-polyacrylamide (PAM).

References

1 C. Wang, P. Chen, Y. Wang, T. Chen, M. Liu, M. Zhang, Y. Fu, J. Xu and J. Fu, *Advanced Functional Materials*, **n/a**, 2204451.

2 W. Chen, T. Lei, T. Qian, W. Lv, W. He, C. Wu, X. Liu, J. Liu, B. Chen, C. Yan and J. Xiong, *Advanced Energy Materials*, 2018, **8**, 1702889.

3 M. Hagen, P. Schiffels, M. Hammer, S. Dörfler, J. Tübke, M. J. Hoffmann, H. Althues and S. Kaskel, *J. Electrochem. Soc.*, 2013, **160**, A1205.

4 J. Xia, W. Hua, L. Wang, Y. Sun, C. Geng, C. Zhang, W. Wang, Y. Wan and Q.-H. Yang, *Advanced Functional Materials*, 2021, **31**, 2101980.

5 T. Lei, W. Chen, W. Lv, J. Huang, J. Zhu, J. Chu, C. Yan, C. Wu, Y. Yan, W. He, J. Xiong, Y. Li, C. Yan, J. B. Goodenough and X. Duan, *Joule*, 2018, **2**, 2091–2104.

6 H. Su, C. Fu, Y. Zhao, D. Long, L. Ling, B. M. Wong, J. Lu and J. Guo, *ACS Energy Lett.*, 2017, **2**, 2591–2597.

7 J. Liao and Z. Ye, *Electrochimica Acta*, 2018, **259**, 626–636.

8 J. Liao, Z. Liu, X. Liu and Z. Ye, *The Journal of Physical Chemistry C*, 2018, **122**, 25917–25929.

9 M. Ling, L. Zhang, T. Zheng, J. Feng, J. Guo, L. Mai and G. Liu, *Nano Energy*, 2017, **38**, 82–90.

10 Z. Huang, L. Wang, Y. Xu, L. Fang, H. Li, B. Zhu and Y. Song, *Chemical Engineering Journal*, 2022, **443**, 136347.

11 Y. Jiao, W. Chen, T. Lei, L. Dai, B. Chen, C. Wu and J. Xiong, *Nanoscale Res Lett*, 2017, **12**, 195.

12 S. Tu, X. Chen, X. Zhao, M. Cheng, P. Xiong, Y. He, Q. Zhang and Y. Xu, *Advanced Materials*, 2018, **30**, 1804581.

13 H. Wang, Y. Wang, P. Zheng, Y. Yang, Y. Chen, Y. Cao, Y. Deng and C. Wang, *ACS Sustainable Chem. Eng.*, 2020, **8**, 12799–12808.